ACS APPLIED NANO MATERIALS

www.acsanm.org

Article

Multicore Manganese Ferrite Nanoparticles for Theranostics

Carlos Eduardo Ribeiro, Marcus Vinícius-Araújo, and Andris Figueiroa Bakuzis*

Cite This: *ACS Appl. Nano Mater.* 2025, 8, 7061−7072

Read Online

ACCESS | Metrics & More | Article Recommendations | Supporting Information

ABSTRACT: Collective behavior mediated by the assembly of nanoparticles (NPs) can result in theranostic applications. Herein, multicore Mn-ferrite-based magnetic nanostructures of various sizes were obtained by tuning the ionic force in the colloidal media, facilitated by a magnetophoresis phase-separation process. The hydrodynamic diameters ranged from 55 nm for the preseparation sample (0 h) to 35 nm at 48 h post separation. X-ray diffraction patterns confirmed the spinel structure. The saturation magnetization decreased from 262.5 kA m^{-1} at 0 h to 111.9 kA m^{-1} at 48 h, indicating a decrease in size. Transmission electron microscopy images corroborate these results but also reveal that lower cluster sizes contained smaller NPs, changing from 15 ± 4 nm at 0 h to 5 ± 2 nm at 48 h. Optical studies revealed a blue-shift phenomenon and a decrease in absorbance with a decrease in size that is consistent with the lower photothermal conversion coefficient, while the band gap energy varied from 1.72 to 2.06 eV due to confinement effects. The longitudinal and transverse (r_2) relaxivities at 20 °C decreased from 20 $mM^{-1}\ s^{-1}$ to 8 $mM^{-1}\ s^{-1}$ and from 750 $mM^{-1}\ s^{-1}$ to 300 $mM^{-1}\ s^{-1}$ from 0 to 48 h, respectively. While the r_2 of the NPs at 0 h decreased at 37 °C to 568 $mM^{-1}\ s^{-1}$, confirming that the clusters are in the motional averaging regime. The results are explained by outer sphere theory and suggest that the magnetic cluster is a thermally sensitive contrast agent with potential for MRI thermometry.

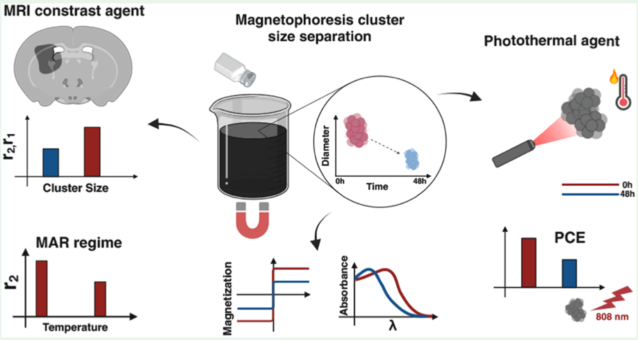

KEYWORDS: *iron oxide, nanomedicine, thermal therapy, thermometry, MRI*

1. INTRODUCTION

The assembly of inorganic nanoparticles (NPs) exhibits distinct optical, electronic, and magnetic properties due to collective behavior, differing from individual NPs.[1−3] Related phenomena include Förster resonance energy transfer, surface plasmon resonance shifts, environment-sensitive MRI effects, and the transition from superparamagnetic to collectively blocked regimes.[1−3] This topic remains of great experimental and theoretical interest for its technological prospective, although many phenomena are still unclear.

From a materials perspective, iron oxide-based nanostructures hold biomedical interest due to their clinical applications. Approved products include treatments for anemia (e.g., Cosmofer, DexIron, Venofer, Feraheme), MRI contrast agents (e.g., Endorem, Feridex, Resovist), and magnetic hyperthermia (e.g., NanoTherm).[4] These nanostructures also show promise in immunotherapy, as their biodegradation releases metallic ions that modulate macrophage polarization, inhibiting tumor growth and metastasis.[5,6]

Thermal therapy modulates innate and adaptive immune responses.[7] Magnetic NPs, approved for hyperthermia, also serve as effective photothermal agents.[8−10] Studies report heat-induced immunogenic cell death, CD8+ T cell and NK cell activation, among other effects.[11−13] Multicore magnetic NPs exhibit strong hyperthermia performance under clinical conditions and evidence of collective magnetic relaxation.[3,14−16] Similar collective behavior enhances MRI contrast when nanostructures assemble compared to isolated NPs.[17]

MRI is essential for theranostics as a noninvasive, nonionizing imaging modality with high spatial resolution. Contrast agents enhance diagnosis and guide clinical decisions, while MRI also enables thermal therapy monitoring, such as MRI thermometry.[18] Gd-based contrast agents are widely used but raise concerns about nephrogenic fibrosis, highlighting the need for safer alternatives.[19] Iron oxide NPs, like magnetite, have been proposed as substitutes, though fast Fe(II) electronic relaxation limits their MRI performance.[20] Doping iron oxide with Mn(II) improves contrast, making Mn-based agents increasingly relevant.[19−21] Mn-ferrite NPs, benefiting from high-spin Mn(II) and Fe(III), are gaining attention for theranostics.[21,22] Studies show NP size reduction can shift contrast properties from *T*2 to *T*1.[23] New synthesis protocols

Received: January 15, 2025
Revised: March 17, 2025
Accepted: March 18, 2025
Published: March 22, 2025

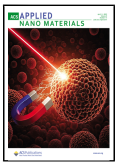

https://doi.org/10.1021/acsanm.5c00309
ACS Appl. Nano Mater. 2025, 8, 7061−7072

are being developed to tune size and surface spin disorder in Mn-ferrite NPs.[24,25]

In fact, high transverse relaxivity correlates with increased magnetization, as seen in Mn- and MnZn-based iron oxide NPs.[17,21,26] These soft ferrites also exhibit strong magnetic hyperthermia properties[26] and show promise for photothermal therapy (PTT).[9−11] Relaxivity depends on NP shape, with octapod geometries outperforming cubic and spherical ones.[17,27] Additionally, NP assembly affects relaxivity, as restricted water diffusion within confined structures enhances it.[17]

This behavior aligns with the outer sphere or motional averaging regime (MAR), relevant for smaller NPs. Under high-field conditions, transverse relaxivity scales with the square of the particle radius and saturation magnetization, and inversely with the diffusion constant.[21,28,29] Field inhomogeneities from NP aggregates of varying sizes and shapes further enhance $T2$ relaxivity,[30] possibly explaining the ultrahigh relaxivity of magnetoliposomes.[31] Optimal transverse relaxivity is linked to cluster formation, with size-dependent transitions from MAR to the static dephasing (SDR) and partial refocusing regime (PRR).[29,32]

Our previous study showed that collective Néel relaxation drives the magnetic hyperthermia of Mn-ferrite multicore nanostructures, as observed via cryogenic TEM.[3] More recently, we reported high transverse relaxivity for similar NPs in various nanocarriers, including magnetoliposomes and hybrid biomimetic vesicles, as well as in magnetic fluids.[22] Here, we investigate the origin of this high relaxivity for theranostic applications. Our hypothesis is that this high relaxivity value is related to cluster size. So, the objective of this research was to evaluate if we were able to select multicore nanostructures of distinct sizes via ionic force-based magnetophoresis-mediated phase separation,[29,33,34] and evaluate their theranostic characteristics, e.g., MRI contrast and PTT performance properties. Through morphological, optical, magnetic, and photothermal characterization, we confirm that the multicore structure size plays a significant role for theranostic applications.

2. MATERIALS AND METHODS

2.1. Chemicals. Manganese(II) chloride tetrahydrate ($MnCl_2 \cdot 4H_2O$) ACS reagent ≥98%, iron(III) chloride hexahydrate ($FeCl_3 \cdot 6H_2O$) ACS reagent ≥97%, iron(III) nitrate nonahydrate ($Fe(NO_3)_3 \cdot 9H_2O$) ACS reagent ≥98%, methylamine solution 40 wt % in H_2O (CH_3NH_2), and sodium citrate tribasic dihydrate ($Na_3C_6H_5O_7 \cdot 2H_2O$) 99% FG were purchased from Sigma-Aldrich (St. Louis, Missouri, USA). Nitrate acid (HNO_3) 65% P.A. was purchased from Cromoline (São Paulo, Brazil).

2.2. Magnetic Nanoparticle Synthesis. The magnetic NPs were synthesized using the coprecipitation method. The precursor ions Mn^{2+} and Fe^{3+} were obtained from 0.5 M manganese chloride tetrahydrate ($MnCl_2 \cdot 4H_2O$) and 1 M iron chloride hexahydrate ($FeCl_3 \cdot 6H_2O$) solutions previously prepared. The medium used was methylamine (CH_3NH_2), prepared by diluting 90 mL of CH_3NH_2 in 400 mL of distilled water. This solution was heated to boiling and maintained under heating. For synthesis, 50 mL of each precursor solution was mixed and heated to 60 °C, then poured into the boiling CH_3NH_2 solution and kept under controlled stirring for 30 min. The particles were magnetically separated, washed three times with distilled water, and prepared for passivation. Passivation was carried out by washing the particles with 50 mL of 0.5 M HNO_3 under stirring, followed by another magnetic separation. The sample was treated with 50 mL of 0.5 M $Fe(NO_3)_3$, heated to boiling for 30 min, and allowed to cool. The particles were washed with acetone three times, and after acetone evaporation, the product was dispersed in water. Then, the NPs were prepared for citrate coating to ensure their colloidal stability at physiological pH. For coating, NPs were diluted in Milli-Q water and sodium citrate ($Na_3C_6H_5O_7$) was added in a ratio of 1 mol of citrate for every 10 mol of iron in the sample. The resulting solution was heated to 80 °C and stirred for 10 min. After being cooled to room temperature, the NPs were magnetically separated again and the supernatant was discarded. The sample was washed three times with acetone and, after complete evaporation of the acetone, the NPs were suspended in Milli-Q water, completing the preparation of the magnetic fluid.

2.3. Phase Separation Method. The stability of the colloidal solution is maintained through the equilibrium of attractive forces (van der Waals and magnetic dipolar) and repulsive forces (steric and electrostatic).[35] Disrupting this balance can promote a "gas-liquid" transition that allows separation of particles of different sizes.[29,33,36,37] This strategy was first reported by Massart et al., who investigated the effect of temperature, magnetic field, and ionic strength.[33] The latter modulates the electrostatic interaction by varying the Debye radius. Increasing ionic strength reduces the range of electrostatic interactions, which was found to be a size-dependent effect.[33] Therefore, 50 mg of solid NaCl were added to a beaker containing 100 mL of citrate coated Mn-ferrite-based magnetic colloid. After adding salt, the solution was left close to the magnet for 48 h, which accelerated the separation of particles/aggregates through a magnetophoresis-mediated process.[34]

2.4. Instrumentation. Several techniques were used to characterize the multicore NPs. X-ray diffraction (XRD) measurements of powder samples for the different separation aliquots (0−48 h) were performed using a Bruker Discover D8 X-ray diffractometer with Cu Kα radiation (wavelength = 0.15 nm). Data were collected in an angular range of 2θ from 10° to 90°, with a step size of 0.01°. Transmission Electron Microscopy (TEM) images were obtained using a JEOL JEM 2100 microscope (Tokyo, JP). The magnetic fluid is diluted in water and a droplet is deposited on the carbon film of the TEM copper grid. Selected area electron diffraction (SAED) images were captured with a camera length of 40 cm. GATAN's Digital Micrograph software was used for the analysis of SAED images, including fast Fourier transformation (FFT), inverse fast Fourier transformation (IFFT), and high-resolution TEM (HRTEM) images. NP size analysis was performed using ImageJ open source software, assuming spherical symmetry for the NPs. A log-normal distribution was applied to the histogram of diameter counts, where the size dispersity is σ and the median diameter D_0:

$$P(D) = \frac{1}{\sqrt{2\pi}\,\sigma D}\exp\left[-\frac{\ln^2 D/D_0}{2\sigma^2}\right] \tag{1}$$

From these two parameters, it is also possible to estimate the mean diameter D_m and its standard deviation ΔD_m using the equations:

$$D_m = \exp\left[\ln(D_0) + \frac{\sigma^2}{2}\right] \tag{2}$$

$$\Delta D = D_m\sqrt{e^{\sigma^2} - 1} \tag{3}$$

Energy-dispersive X-ray spectroscopy (EDS) analysis was performed using an Oxford Instruments X-MaxN detector attached to a Jeol JSM-IT300LV scanning electron microscope (SEM), operating at a 15 kV electron acceleration voltage. Room-temperature magnetization data were obtained using a VSM model EV9 from ADE Magnetics (MicroSense, USA) with field range ±2 T. The magnetization technique was used to determine the saturation magnetization of the NPs and the volume fraction of magnetic particles of the prepared samples.[22] Basically, the specific saturation magnetization (magnetic moment per unit mass) of the sample was measured for both the NP powder and the fluid. The volume magnetization is obtained by multiplying the specific magnetization by the NP density for the powder and by the water density for the fluid (due to the low NP concentration). The ratio of the volume magnetizations of the fluid and the powder corresponds to the magnetic particle volume fraction. Notably, multiplying the NP volume fraction by the NP density gives the mass concentration of NPs per unit volume. Therefore, we can calculate [Fe + Mn] in mM (see the MRI Investigation section).

The dynamic light scattering (DLS) technique was used to measure the hydrodynamic diameters of the collected aliquots. The measurements also provided the polydispersity index (PDI) of the samples. Measurements of the hydrodynamic size distribution of the NPs were performed using a Zetasizer Nano S ZEN 1600 (Malvern Panalytical, Westborough, MA, USA). Each measurement was carried out in triplicate at a controlled temperature of 25 °C. The absorbance data were acquired using a Kasvi K37-UVVIS spectrophotometer. The energy band gap of the Mn-ferrite NP is determined using the experimental UV−vis spectroscopy data assuming a direct transition semiconductor ($n = 1/2$) and Tauc's relation[38]

$$\alpha \cdot h\nu = A\cdot(h\nu - E_g)^n \tag{4}$$

α is the absorption coefficient, hv is the photon energy, A is a constant, while E_g is the band gap energy. So, using the absorbance data and converting to Tauc's plot $(\alpha \cdot h\nu)^2$ versus $h\nu$, it is possible to determine the E_g by fitting the linear part of the graph.

2.5. Photothermal Study. PTT experiments were performed using a diode laser at 808 nm wavelength, model Laser iZi 808, bought from LASERline (São Paulo, Brazil). The surface temperature was monitored using an infrared thermal camera bought from FLIR, model SC620 (Wilsonville, United States). A region of interest (ROI) centered at the laser spot on the sample was used to report the mean temperature during PTT. The experiments were carried out using cuvette and droplet methods.[39,40] For the cuvette experiments, 200 μL aliquots of each sample were taken at a concentration of 2 mg/mL. For the droplet method, 13 μL droplets were measured at a concentration of 0.2 mg/mL.

The photothermal conversion efficiency (PCE) of a material can be determined using the Roper method,[39] where the sample is heated until it reaches thermal equilibrium. The PCE is obtained using the equation:

$$\text{PCE} = \frac{hS(T_{\max} - T_0) - \dot{Q}_0}{P(1 - 10^{-A_\lambda})} \tag{5}$$

The term hS is derived from fitting the cooling curve, $\dot{Q}_0$ represents the heat absorption rate by the sample holder and the carrier liquid (water), P is the laser power, A_λ is the absorbance at the specified wavelength, $T_{\max}$ is the maximum temperature reached, and T_0 is the room temperature.[10] The absorption curves were obtained using a Cary 50 UV−vis spectrophotometer (Varian Inc., Palo Alto, CA, USA) at room temperature in the 400−1000 nm wavelength range.

Recently, Pasciak et al.[40] introduced a new parameter to assess the heating performance, the external photothermal efficiency parameter, which is defined as ePCE = a_λPCE. In this expression, a_λ is given by $a_\lambda = A_\lambda/cL$, where A_λ represents the absorbance at a specific wavelength, c is the mass concentration (mg/mL), and L is the optical path (cm).[40] The ePCE value is estimated using the droplet method.

2.6. MRI Investigation. The MRI measurements were performed at 20 °C with the 1.0T M7 Compact MRI system from Aspect Imaging. The samples were diluted in 14 mL of water from their original batch to obtain concentrations in the range of 0.06 mM to 0.15 mM of [Fe + Mn], to prevent susceptibility-related artifacts in image reconstruction. The determination of $T1$ used a Snapshot Flash sequence, that is, an inversion recovery pulse sequence with a short echo time (TE = 1.9 ms), to reduce the influence of $T2$ on the intensity of the MRI signal. The Snapshot Flash sequence utilizes a Gradient Recalled Echo pulse, enabling rapid $T1$ acquisition due to its short repetition time, resulting in a total measurement time of 8 min. This method is well established for $T1$ measurements and was chosen for use with our equipment.[41,42] Inversion times (TI) ranged from 50 to 800 ms with repetition time TR = 71 ms, flip angle FA = 6° and voxel dimension of $(0.75 \times 0.75 \times 2)$ mm^3. $T1$ can be determined using the equation below[43]

$$S = |A - B\,e^{-TI/T1}| \tag{6}$$

$T2$ is obtained using a spin echo pulse sequence with long repetition time (TR = 4000 ms), to minimize the effect of longitudinal relaxation $T1$ on the signal. Same voxel dimension was used. Echo times ranged from 7.5 to 25 ms. $T2$ is determined using

$$S = S_0\,e^{-TE/T2} \tag{7}$$

The longitudinal relaxivity r_1 and transverse relaxivity r_2 are obtained by fitting the data $Ri = 1/Ti$ as a function of contrast agent concentrations (mM) through the equation:

$$1/Ti = r_i\cdot[C] + 1/Ti_0 \tag{8}$$

$Ri_0 = 1/Ti_0$ is the solvent relaxivity.

3. RESULTS AND DISCUSSIONS

Figure 1 shows a schematic representation of the ionic strength magnetophoresis-mediated separation protocol used to obtain size-differentiated NPs. The phase separation process has been successfully utilized by others for this purpose.[29,33,36,37] The magnetic colloid sample is positioned 7.5 cm from the top of the magnet, where magnetophoresis is induced by a magnetic field gradient of 0.1 T·m^{-1}. Initially, the 0-h aliquot sample is separated without exposure to the magnet or alteration of the ionic force. Subsequently, the sample is diluted in 150 mL of Milli-Q water and placed near the magnet, followed by the addition of 25 mg of sodium chloride. The introduction of salt modifies the ionic force, promoting phase separation.[33] The aliquots are then collected from the top of the colloid after 1-h, 2-h, 3-h, 24-h, and 48-h separation intervals. Since magnetophoresis is more effective for larger particles or clusters, smaller sizes are expected at the top of the colloid with extended separation times.[34]

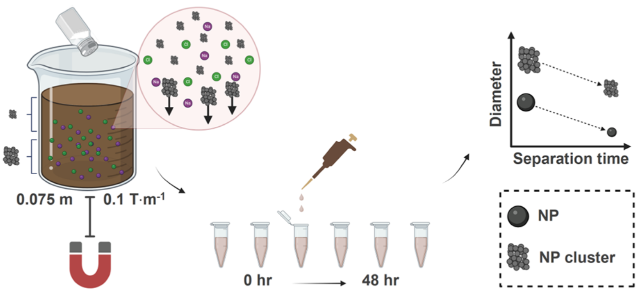

Figure 1. Schematic representation of the ionic strength separation protocol facilitated by magnetophoresis for obtaining size-differentiated particles/clusters. Samples were collected in different periods to better explore the separation time influence on NP diameter and cluster size.

The first experimental evidence of the success of the size separation protocol emerged from the magnetic characterization study. Figure 2a displays the magnetization curves measured at room temperature for all aliquots. Some samples showed similar magnetization data. These curves exhibit superparamagnetic-like behavior (no hysteresis) and a systematic decrease in saturation magnetization with increasing separation time. M_s decreased from 262.5 kA·m^{-1} at 0 h to 111.9 kA·m^{-1} at 48 h. Table 1 lists the values obtained for each aliquot. The reduction in saturation magnetization supports a decrease in NP diameter over longer separation periods.[44] A core−shell model can be applied to explain this apparent decrease in magnetization by assuming a nonmagnetic shell layer (caused by a noncrystalline shell or surface spin disorder)

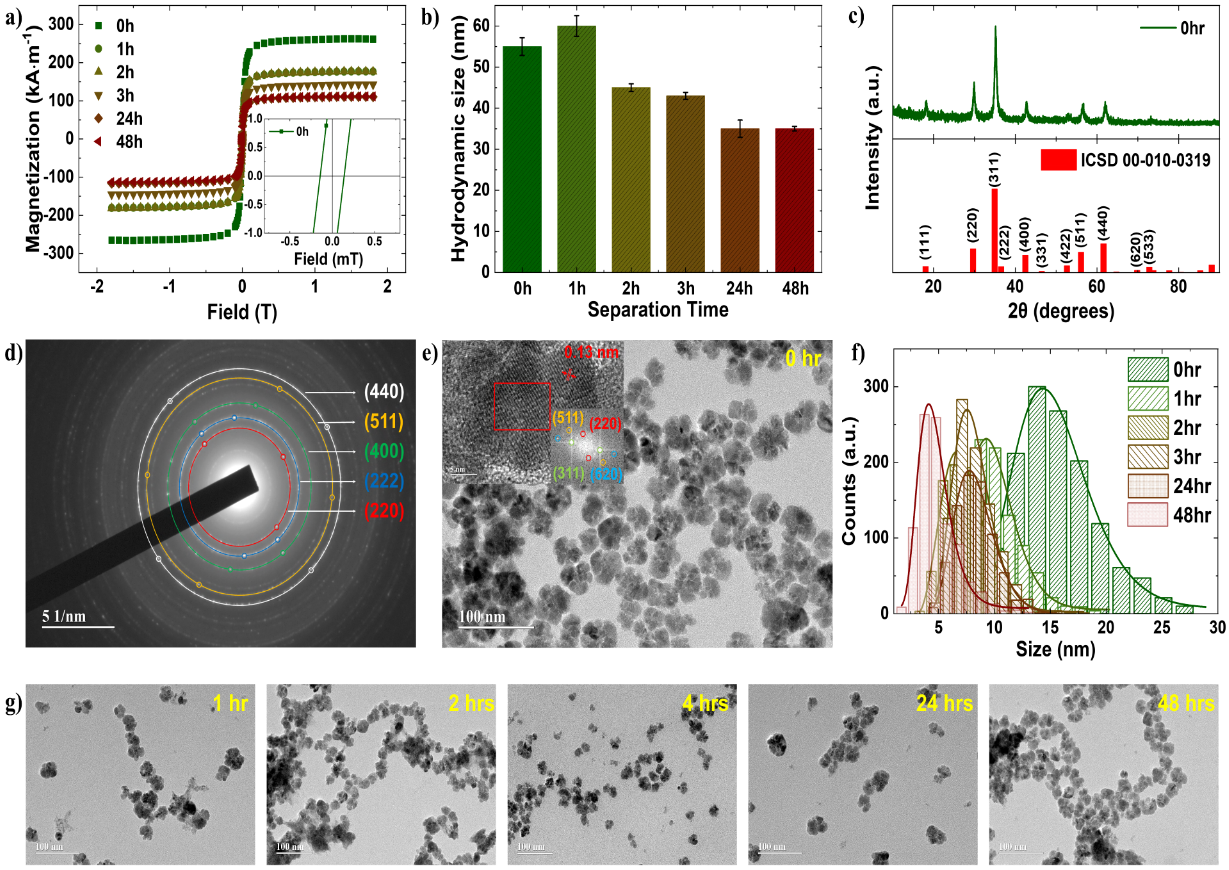

Figure 2. Structural, magnetic, and morphological characterization of $MnFe_2O_4$-based NPs. (a) Room temperature magnetic hysteresis curves for all aliquots. (b) Hydrodynamic sizes measured by Dynamic Light Scattering. (c) Powder XRD pattern of the $MnFe_2O_4$-based NPs aliquot at 0-h confirming the spinel structure. (d) SAED ring patterns of $MnFe_2O_4$-based NPs at 0-h confirming the spinel structure. (e) TEM image of 0-h $MnFe_2O_4$ NPs, showing a multicore-like morphology. Inset shows a high-resolution TEM image of a multicore NP with corresponding FFT and IFFT analysis. (f) Size histograms of NPs in the cluster fitted with a log-normal distribution. (g) TEM representative images of the multicore $MnFe_2O_4$-based NPs for aliquots at 1-h, 2-h, 3-h, 24-h, and 48-h separation intervals.

Table 1. Structural, Optical and Magnetic Properties of Multicore $MnFe_2O_4$ NPs at Different Separation Intervals[a]

Sample	D_{TEM} (nm)	D_{XRD}^{SR} (nm)	D_{XRD}^{HW} (nm)	M_s (kA·m^{-1})	D_{DLS} (nm)	E_g (eV)	κ_{shell} (nm)	ξ (mV)
0 h	15 ± 4	14.9	12.5	262.5	55	1.720	1.50	−30.3
1 h	10 ± 2	12.9	10.3	177.3	60	1.856	1.48	−25.0
2 h	7 ± 2	13.5	11.6	177.0	45	1.856	1.06	−26.1
3 h	8 ± 2	12.5	10.3	143.0	43	2.044	1.40	−22.0
24 h	8 ± 2	12.4	10.6	111.1	35	2.042	1.63	−35.4
48 h	5 ± 2	13.0	11.4	111.9	35	2.065	0.97	−32.8

[a] D_{TEM}: TEM mean size, D_{XRD}: X-ray diffraction crystallite size (SR: Scherrer relation, HW: Halder−Wagner analysis), M_s: saturation magnetization, D_{DLS}: hydrodynamic size, E_g: band gap energy, κ_{shell}: shell thickness, ξ - zeta potential.

and a core magnetization equal to the bulk material's value (500 kA·m^{-1}).[45,46] Table 1 also shows the shell thickness (κ_{shell}) values obtained with this model, varying from 1 to 1.5 nm, consistent with one to two ferrite unit cells. Although surface effects are an important contributor, cation redistribution within the crystalline structure can also significantly impact M_s and may depend on particle size, influencing the estimation of κ_{shell}.[47] However, the results align with a reduction in size.

Figure 2b shows the hydrodynamic sizes measured using the dynamic light scattering technique, revealing a decrease in cluster size within the liquid carrier as the separation time increases. The size decreased from 55 nm at 0-h to 35 nm at 48-h. The exception for this behavior was the sample at 1 h, that showed a higher hydrodynamic size, 60 nm. We suspect that this happened due to hydrodynamic interactions, that might induce fluid movement at the beginning of the separation process. Zeta potential measurements (see Figure S1) are consistent with a citrate surface coating, showing slight variations (see Table 1). Figure 2c presents the powder XRD pattern of the 0-h aliquot, confirming the spinel crystal structure as evidenced by the reference ICDD No. 00-010-0319. The XRD patterns for other samples are provided in Figure S2. The crystallite size was estimated using Scherrer's (SR) equation and Halder−Wagner (HW) analysis (see Table 1), showing a decrease from 14.9 nm for the 0-h sample to 13 nm for the 48-h aliquot calculated using Scherrer's equation, and from 12.5 nm for the 0-h sample to 11.4 nm for the 48-h

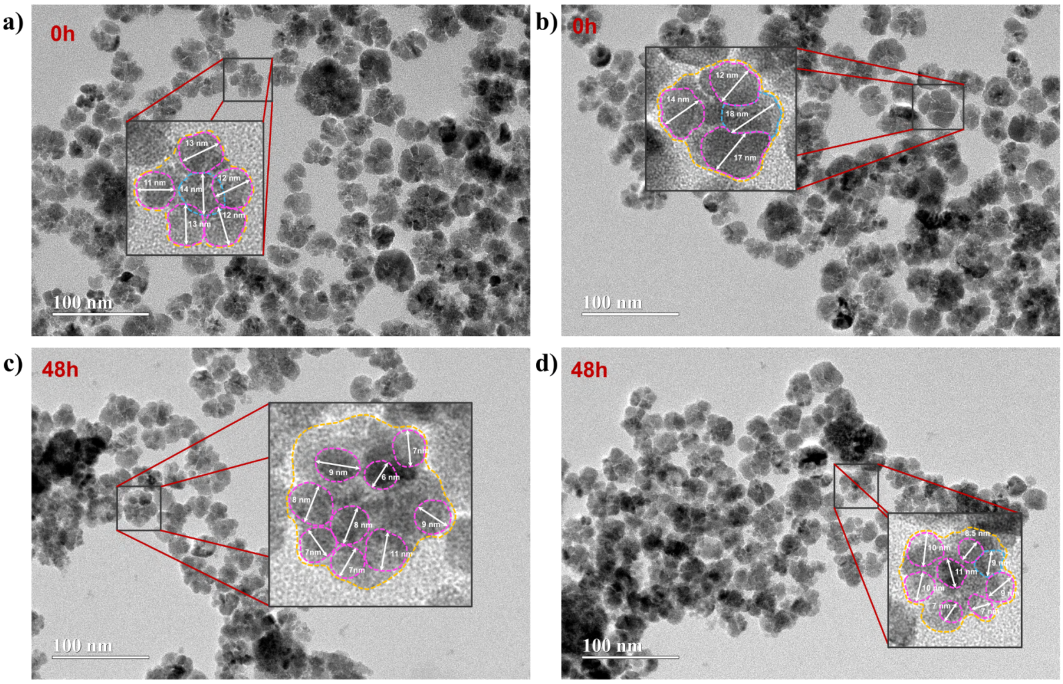

Figure 3. TEM analysis of Mn-ferrite multicore NPs at different separation intervals. (a) and (b) Representative TEM images of the Mn-ferrite multicore NPs for the 0-h sample, while (c) and (d) correspond to the 48-h aliquot. The insets show a cluster formed by NPs with distinct diameters.

aliquot using the Halder–Wagner formalism. The determination of crystallite sizes via linear regressions using the Halder–Wagner formalism can be seen in Figure S3. TEM data were also collected for structural and morphological analysis. Figure 2d displays the SAED patterns for manganese iron oxide-based NPs. The analysis of the SAED ring patterns confirms the cubic spinel structure, with corresponding planes consistent with the reference pattern: (220) → 0.29 nm, (222) → 0.24 nm, (400) → 0.20 nm, (511) → 0.16 nm, and (440) → 0.14 nm. The planes are consistent with the peaks observed in the XRD pattern.

Figure 2e presents a representative TEM image of the 0-h sample, clearly showing multicore-like nanostructures. This multicore morphology is attributed to the synthesis protocol.[3] It is important to note that during the drying process, the magnetic particles in the colloid droplet tend to aggregate; however, they generally form "fractal-like" structures distinct from those observed for this sample (see, for example, refs [34 and 45]). Additionally, several cluster sizes observed in the TEM images are consistent with the values reported by DLS. The inset shows a HRTEM image of the multicore nanostructure, where distinct NPs within the cluster are visible. A selected area of the image was analyzed using FFT, revealing planes corresponding to different orientations of the inverse spinel Mn-ferrite NPs with interatomic distances: (220) → 0.31 nm, (311) → 0.26 nm, (511) → 0.15 nm, and (620) → 0.13 nm. The IFFT analysis further confirmed interplanar distances within the multicore structure consistent with the crystal structure. Overall, the HRTEM data corroborate the findings from the SAED and XRD analyzes.

Figure 2f shows the size distribution of NPs within the clusters from aliquots separated at intervals of 0-h, 1-h, 2-h, 3-h, 24-h, and 48-h (see discussion below). The size histograms are fitted using a log-normal distribution, revealing a decrease in the mean core diameter over time. The mean core diameter and size dispersity were determined as follows: $D_m = 15 \pm 4$ nm with $\sigma = 0.22$ for the 0-h aliquot, $D_m = 10 \pm 2$ nm with $\sigma = 0.21$ for the 1-h aliquot, $D_m = 7 \pm 2$ nm with $\sigma = 0.28$ for the 2-h aliquot, $D_m = 8 \pm 2$ nm with $\sigma = 0.21$ for the 3-h aliquot, $D_m = 8 \pm 2$ nm with $\sigma = 0.22$ for the 24-h aliquot, and $D_m = 5 \pm 1$ nm with $\sigma = 0.30$ for the 48-h aliquot. Figure 2g shows representative TEM images of the other aliquots. Multicore magnetic nanostructures are visible in all samples.

Determining the size of NPs within the clusters can be challenging. We consider this procedure an approximation, strongly supported by magnetization data and optical studies (see below). Figure 3 presents representative TEM images of the Mn-ferrite multicore nanostructures for the 0-h aliquot (a and b) and the 48-h aliquot (c and d). The insets show a cluster image formed by NPs with distinct diameters. The images indicate that the NPs are larger at 0-h compared to the 48-h aliquot, although some larger particles are still observed in the latter. This observation may explain the larger crystallite size obtained by XRD compared to the TEM size determined for this sample (see Table 1). The estimated values of XRD decreased by around 2 nm with the HW analysis in comparison to Scherrer's estimation. However, there is still a discrepancy because in the TEM images we are evaluating the clusters of NPs, and only smaller NPs are more easily identified. Anyway, it is notable that the crystallite size decreases from 0-h to 48-h. This behavior is expected because XRD tends to favor larger particle sizes. Additional images supporting the histograms reported in Figure 2e are provided in the Supporting Information (Figures S4 and S5).

In summary, our TEM analysis indicates that Mn ferrite NPs tend to form clusters. Within these clusters, the larger NP appears to be attached to smaller NPs. The similar XRD size values in Table 1 suggest that the larger NP in each sample's cluster is of comparable size, as this technique weights higher NP size. In contrast, the magnetic characterization considers all

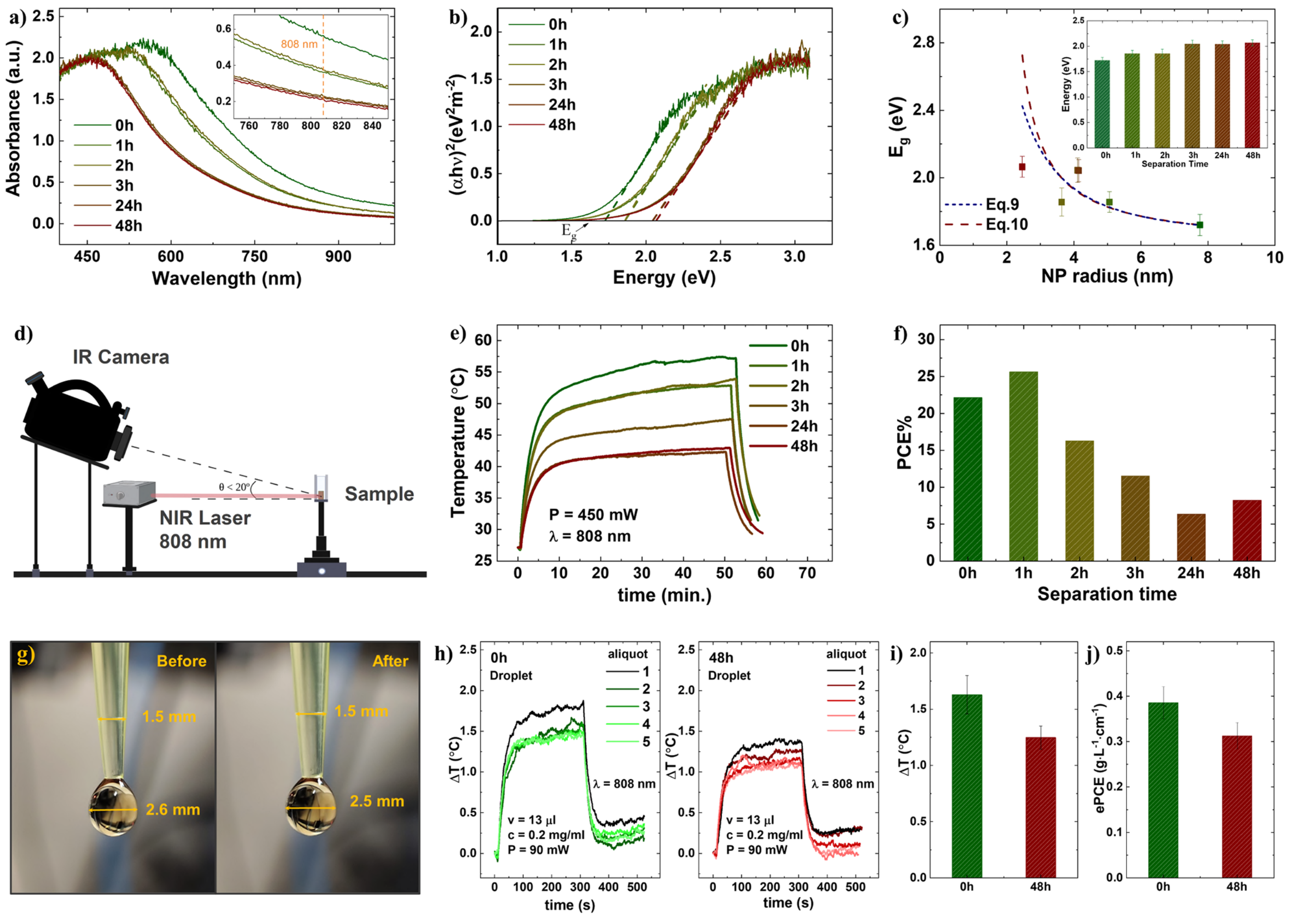

Figure 4. Optical properties and PTT performance of Mn-ferrite multicore NPs. (a) Absorbance curve for all aliquots. Inset shows data near 808 nm. (b) Tauc's plot data for all aliquots. (c) The inset shows the band gap energy determined fitting the linear region of (b). Symbols in (c) represent the band gap energy as a function of NP radius determined by TEM, while the lines are the best fit using eqs 9 and 10. (d) Experimental setup of the PTT study for the cuvette method. (e) Temperature profile during PTT for all aliquots at 450 mW and 808 nm. (f) PCE for all aliquots determined using Roper's method. (g) Representative image of the droplet experiment before and after PTT. (h) Temperature profile during PTT with the droplet method for several aliquots of samples 0-h and 48-h at 90 mW and 808 nm. (i) Mean temperature variation for the 0-h and 48-h sample aliquots. (j) ePCE for the 0-h and 48-h sample aliquots.

NPs in the cluster. Notably, the smaller magnetization value correlates with the lower NP size estimated by TEM. Therefore, these results are consistent with the TEM analysis and reinforce the success of the separation process.

The Mn and Fe content in the NPs was estimated using EDS for the 0 h sample. To improve the quantification of these ions with this technique, the NPs were pressed under 2.5 tons, and the resulting film was analyzed. Three areas of the film were examined by EDS, and the Fe and Mn concentrations were determined (see Figure S6). We found 72.2 ± 0.2% for Fe and 28.1 ± 0.6% for Mn. At this point, it is important to recall that the NP synthesis includes a passivation process that enriches the Mn-ferrite NP surface with Fe, resulting in a core−shell-like nanostructure. Assuming a shell thickness of 0.8 nm, the percentage of Mn can be estimated as $\%\text{Mn} = \frac{1}{3}\left(\frac{D_{\text{Core}}}{D_{\text{NP}}}\right)^3$. This yields a Mn content of 23.7%, which is close to the experimental value. On the other hand, the experimental data can be explained by assuming a shell thickness of 0.4 nm.

The optical study further supports the observed size decrease. Figure 4a shows the absorbance spectra for all samples, where a peak position blue-shift is evident with increasing separation time. The inset shows the absorbance near the laser excitation wavelength (808 nm), clearly demonstrating a decrease in absorption with longer separation periods. The absorption coefficient values were extracted, and the absorbance data were converted to the Tauc's plot $(\alpha\cdot h\nu)^2$ vs $h\nu$, as shown in Figure 4b. By fitting the linear part of the graph, the energy band gap of the Mn-ferrite NPs was calculated, as presented in the inset of Figure 4c and Table 1. The E_g value increased from 1.72 eV at 0-h to 2.06 eV for the 48-h aliquot, consisted with confinement effects because of size decrease.

Indeed, the band gap energy radius dependence is usually evaluated with[48,49]

$$E_g(r) = E_g(\text{bulk}) + \frac{h^2}{8r^2}\left(\frac{1}{m_h^*} + \frac{1}{m_e^*}\right) - 0.248E_{\text{Ry}}^* \qquad (9)$$

where h is Planck constant, m_h^* and m_e^* are the effective mass of holes and electrons respectively, and $E_g(\text{bulk})$ is the bulk energy band gap, while E_{Ry}^* is the bulk exciton binding energy. To fit the experimental data one can use two fitting parameters,

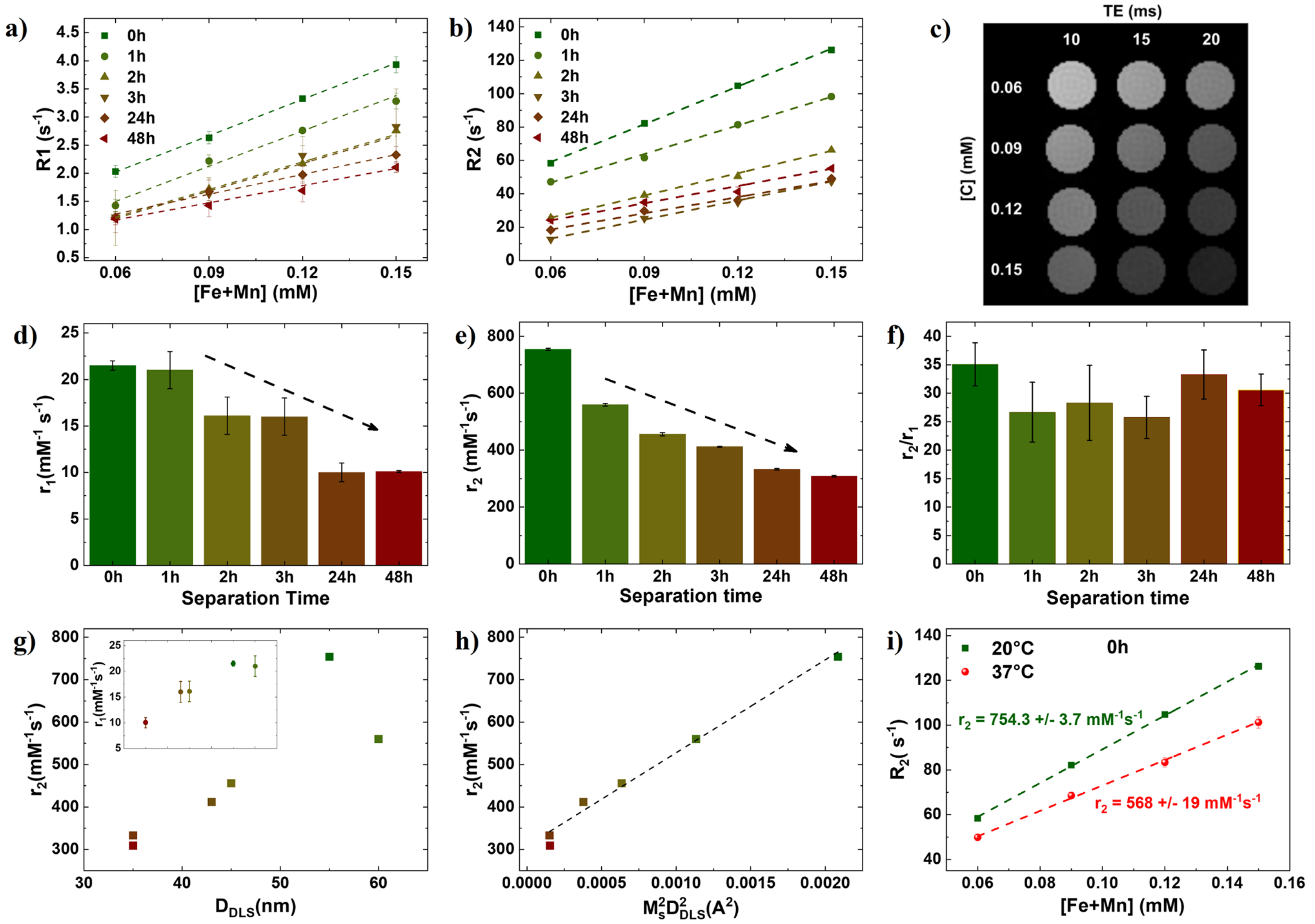

Figure 5. Magnetic relaxometry analysis of Mn-ferrite multicore NPs. (a) $R1$ data as a function of NP concentration ([Fe + Mn] in mM) for all samples. (b) $R2$ data as a function of NP concentration ([Fe + Mn] in mM) for all samples. In (a) and (b) symbols are data while lines are the best fit using eq 8 to extract r_1 and r_2, respectively. (c) Representative $T2$ images for the 0-h aliquot at spin echo times TE = 10, 15, and 20 ms and different NP concentration. (d) r_1 relaxivities, (e) r_2 relaxivities, and (f) r_2/r_1 ratio for aliquots at 0-h, 1-h, 2-h, 3-h, 24-h, and 48-h separation intervals. (g) r_2 as a function of hydrodynamic size. Inset, r_1 as a function of hydrodynamic diameter. (h) r_2 as a function of the square of the product of the hydrodynamic diameter and the particle saturation magnetization. The dotted line represents the fit of r_2 with eq 11, confirming that the clusters are in the outer sphere regime. (i) $R2$ data of the 0 h sample as a function of NP concentration ([Fe + Mn] in mM), at 20 °C and 37 °C.

a_1 and b_1, using $E_g(r) = a_1 + b_1/r^2$. Recent research also suggested an empirical size dependence expression for $E_g(r)$ inspired on tight binding calculations where[50,51]

$$E_g(r) = E_g(\text{bulk}) + \frac{1}{a_2r^2 + b_2r + c_2} \tag{10}$$

Figure 4c shows our experimental results (symbols) of the energy band gap as a function of NP radius (determined by TEM), while the solid lines are the best fit for both models. Using eq 9 returns a_1 of 1.64 ± 0.07 eV, while for eq 10 one obtain E_g(bulk) of 1.61 ± 0.04 eV. The estimated bulk band gap energy values are consistent with the literature for this type of NP.[52] The good agreement between data and theory corroborates with confinement effects.[48,50]

Figure 4d shows the experimental setup for the PTT study using the cuvette method. Photothermal assays were performed with an 808 nm laser at 450 mW, using a concentration of 2 mg/mL and a total volume of 200 μL. The irradiation lasted for 50 min, followed by a cooling period of 5 min. The temperature was monitored with a thermal camera. As shown in Figure 4e, samples with longer separation times exhibited a lower heat generation capacity, resulting in a lower photothermal conversion efficiency (Figure 4f) calculated using Roper's method.[9,39] These findings align with the absorbance results, which also decreased in samples with longer separation times. However, the PCE determination and Roper's method are topics of ongoing debate in the literature.[40] Specifically, there is criticism regarding the use of the cuvette method to determine PTT efficiency. Pasciak et al.[40] proposed a new external photothermal efficiency parameter (ePCE) for evaluating and comparing different materials for PTT application. The ePCE value is estimated using the droplet method.

Figure 4g shows a representative image of the droplet experiment before and after PTT for the 0-h aliquot. A small volume change is observed, but this does not affect the determination of PTT efficiency. In this method, it is crucial to minimize droplet evaporation; therefore, a lower NP concentration and lower laser power are used compared to those in the cuvette method. Figure 4h presents several experiments for the 0-h and 48-h aliquot samples, where the temperature variation is low due to these experimental conditions. The method is highly sensitive to the environment conditions, so five distinct experiments are carried out for each sample. Figure 4i shows the mean temperature reached by both aliquots, confirming that the 0-h sample exhibits a higher temperature variation than the 48-h aliquot. Similarly, the ePCE value is higher for the 0-h sample, as shown in Figure 4j. The values obtained for Mn-ferrite multicore nanostructures are comparable to and approximately four times higher than previous literature reports for maghemite NPs.[40] These results clearly demonstrate that this ferrite is highly effective for PTT applications, as already shown *in vivo* by our group.[11,22]

The contrast performance of the NPs was characterized using a preclinical 1T MRI system. Longitudinal relaxation was evaluated with the Snapshot Flash sequence (TR = 71 ms, TE = 1.9 ms, TI = 50−800 ms, FA = 6°), while transverse relaxation was evaluated using spin echo sequences (TR = 4000 ms, TE = 7.5−25 ms) at multiple echo times. Figure S7a shows the MRI signal intensity as a function of inversion time (TI) for the 0-h multicore $MnFe_2O_4$ nanostructure. Symbols represent experimental data at various concentrations, and the line is the best fit to the eq 6. Each curve allows for the extraction of the $T1$ values. Figure 5a shows the concentration dependence behavior of $1/T1$, that yields a longitudinal relaxivity (r_1) of 21.5 $mM^{-1}\ s^{-1}$ for the 0-h sample. Similarly, Figure S7b illustrates the signal intensity versus spin−echo time (TE) for the 0-h aliquot. Symbols indicate experimental data at various concentrations of NP, while the line represents the best fit to the eq 7. The results for the other aliquots appear in Figures S8, while Tables S1 and S2 show all the $T1$ and $T2$ values extracted from these analyzes. Figure 5b shows the analysis of $1/T2$ versus particle concentration, that from the linear fit provides the transverse relaxivity r_2, found to be 754.3 $mM^{-1}\ s^{-1}$ for the 0-h sample. Figure 5c displays typical images obtained for all 0-h samples at a spin echo time of 10−20 ms. A similar analysis was performed for each aliquot at the 1-h, 2-h, 3-h, 24-h, and 48-h separation time intervals, as shown in Figures S7 and S8. The r_1 relaxivities in Figure 5d indicate a decrease in the longitudinal relaxivity with increasing separation time, from 21.5 $mM^{-1}\ s^{-1}$ for the 0-h aliquot to 10 $mM^{-1}\ s^{-1}$ for the 48-h aliquot. For the transverse relaxivity, shown in Figure 5e, a similar decrease in r_2 relaxivity is observed with separation time, from 754.3 $mM^{-1}\ s^{-1}$ for the 0-h aliquot to 309 $mM^{-1}\ s^{-1}$ for the 48-h aliquot. The ratio of transverse to longitudinal relaxivity, presented in Figure 5f, indicates that the aliquots serve as T2 contrast agents. The 0-h result aligns with a recent publication of our group[22] using NPs of the same composition. Moreover, the correlation of r_2 with increasing separation times supports a reduction in particle diameter over time.[23]

Figure 5g shows r_2 as a function of hydrodynamic size, while the inset shows the r_1 data. The longitudinal relaxivity increased the higher the cluster size, while the transverse showed an apparent peak. The presence of a peak and optimum hydrodynamic sizes has been investigated before,[32] and is predicted by the quantum-mechanical outer sphere theory that establishes three regimes as a function of size.[21,29] At low particle/aggregate size the relaxivity is governed by the MAR, while optimum relaxivity is found at the SDR, followed by a decrease the higher the cluster size for the PRR.[21,32] The result of Figure 5g suggests that maximum relaxivity is observed for the 0-h sample that had a cluster size of 55 nm. However, it should be emphasized that the NPs forming the clusters have different sizes, as evidenced by several techniques before (see Table 1). This situation is completely different from the interesting experiment of Pöselt et al.[32] that tunes the cluster size by using distinct lipids (micelles) but maintains the diameter of the magnetic NPs forming the cluster. In that study, the authors evaluated clusters formed by core NPs of distinct sizes, ranging from 4 to 13 nm, while the hydrodynamic sizes were tuned from 30 to 230 nm. In our case, the ionic force magnetophoresis mediated size process results in the separation not only of clusters of different size, but we showed evidence that the NPs in the cluster are also different. This suggest that the graph is representing an apparent peak. There are two ways to check this hypothesis: (i) apply the relaxivity theory for clusters, and (ii) check if the maximum value obtained is temperature dependent.

In the MAR regime, under high field conditions, the transverse relaxivity is given by,[21,28,29]

$$r_2 = \frac{16}{45}\nu_{\mathrm{mat}}\tau_{\mathrm{D}}\cdot\Delta w^2 \tag{11}$$

$\nu_{\mathrm{mat}} \approx 1.5 \times 10^{-5}\ \mathrm{m^3 \cdot mol^{-1}}$ for isolated Mn-ferrite NPs.[29] For a cluster, one has $\tau_{D_c} = d_{\mathrm{cluster}}{}^2/4D$, which is the diffusion correlation time, while $\Delta w_c = \gamma_{\mathrm{H}}\mu_0 M_{\mathrm{cluster}}/3$ is the Larmor frequency shift of the proton at the equator of the cluster.[28] Here, d_{cluster} is the cluster diameter (estimated as hydrodynamic size), D is the water diffusion coefficient, γ_{H} = $2.67513 \times 10^8\ \mathrm{rad \cdot s^{-1} \cdot T^{-1}}$ is the proton gyromagnetic ratio, μ_0 = $4\pi \times 10^{-7}\ \mathrm{T \cdot m \cdot A^{-1}}$ the vacuum magnetic permeability, and $\nu_{\mathrm{mat,c}} \approx 1.5 \times 10^{-5}\ \mathrm{m^3 \cdot mol^{-1}}/\phi_c$, with ϕ_c being the NP volume fraction in the cluster. The cluster magnetization is $M_{\mathrm{cluster}} = \phi_c M_s \cdot \langle \cos\theta_c \rangle$, where M_s is the particle magnetization and $\langle \cos\theta_c \rangle$ is the mean value of the reduced cluster magnetization. For noninteracting NPs in the cluster, assuming NPs at the superparamagnetic regime, this value should correspond to the Langevin function, which at high field condition gives $\langle \cos\theta_c \rangle \approx 1$. However, for interacting particle systems, due to magnetic dipole and/or surface exchange interactions, as well as the random configuration of anisotropy axes among the NPs forming the cluster, these values are expected to lie between 0 and 1.

It is possible to show that the MAR regime applied to a cluster gives

$$r_2 = \left[\frac{4\mu_0{}^2\gamma_{\mathrm{H}}{}^2\nu_{\mathrm{mat}}}{405D}\right]\delta_c M_s{}^2 d_{\mathrm{cluster}}{}^2 \tag{12}$$

with $\delta_c = \phi_c\langle \cos\theta_c \rangle^2$. Figure 5h shows the transverse relaxivity r_2 as a function of $M_s{}^2 D_{\mathrm{hyd}}{}^2$. Symbols represent the experimental data listed in Table 1, while the line is the linear fit. The excellent agreement of the model with the experimental data suggests that all samples are in the MAR regime. The experimental slope is $2.19 \times 10^5\ \mathrm{mM^{-1}\ s^{-1}\ A^{-2}}$, which can be compared with the theoretical value from eq 12, that is $8.27 \times 10^6 \delta_c\ \mathrm{mM^{-1}\ s^{-1}\ A^{-2}}$. If the NPs inside the cluster could be approximated as noninteracting systems, then $\delta_c = \phi_c$ = 0.026. However, this is a nonphysical value for such clusters, meaning that $\langle \cos\theta_c \rangle \neq 1$. Since the MAR regime is expected to be valid for $\Delta w_c \cdot \tau_{D_c} < 1$, a critical value for ϕ_c^* and θ_c^* can be estimated for the samples. In particular, for the 0-h aliquot, considering the experimental slope and the critical MAR condition, it is possible to obtain physical values for the interacting model, $\phi_c^* = 0.32$ and $\langle \cos \theta_c^* \rangle = 0.286$, which again corroborates with our findings.

The result of the transverse relaxivity for the 0-h aliquot is 750 mM^{-1} s^{-1}. The value is within the highests in the literature, but within theoretical expectations due to the size of the NPs, the low temperature (20 °C), and the formation of clusters.[17,29] Indeed, the outer sphere theory indicates that maximum/optimum transverse relaxivity $r_{2,\max}$ should be found at the SDR regime, where the value is approximately given by[29]

$$r_{2,\max} \approx \frac{2\pi\gamma_H\mu_0 v_{mat} M_s^{core}}{9\sqrt{3}} \tag{13}$$

Assuming the bulk magnetization of Mn-ferrite is 500 kA m^{-1},[46] one can estimate $r_{2,\max}$ = 1016 mM^{-1} s^{-1}. This maximum value is higher than the one obtained for the 0-h multicore Mn-ferrite nanostructure. Furthermore, additional proof that the 0-h sample is not in the SDR regime could be obtained by checking for temperature effects. Note that varying the temperature by around 10 degrees for ferrite-based NPs should not affect the r_2 values in the SDR regime, as previously demonstrated by others,[28] since the variation in magnetization over such a short temperature range might not be significant, given that the critical temperature of Mn-ferrite is typically found in the range of 570−680 K.[53−55] On the other hand, contrast agents in the MAR regime should have a temperature dependence due to variation of the water diffusion constant with temperature.

Figure 5i shows the relaxivity as a function of NP concentration for the 0-h aliquot sample at two distinct temperatures, 20 °C and 37 °C. The linear fit of these data revealed a transverse relaxivity value of 754 mM^{-1} s^{-1} at 20 °C, while at higher temperature, 37 °C, it decreased to 568 mM^{-1} s^{-1}. In Figures S9, one can find the data obtained to extract the points in Figure 5i. The result undoubtedly indicates that r_2 decreased with increasing temperature, where the ratio varied by ∼33% . It is well-known that M_s is temperature dependent, but estimation of the ratio using data of the literature with similar NPs suggest a variation of ∼4% for the case of SDR and ∼8% in the MAR regime, that is far below the experimental observation.[55] So, the behavior correlates with the increase of the water diffusion constant for higher temperatures, that for pure water would result in a ratio increase of ∼53%, from 2.025 $\mu m^2/mm$ at 20 °C to 3.094 $\mu m^2/mm$ at 37 °C.[56] The ratio value is higher than the experiment, but maybe the explanation arises on the modification of the water diffusion constant close to clusters or confined arrangements where surface coating temperature effects might play a role.[17] These analysis is consistent with a recent study of the literature that evaluated the NMR line width and T2 maps temperature dependence of magnetite-based colloids.[57] Basically, our results suggest that the Mn-ferrite multicore nanostructure might have applications for MRI thermometry,[8,18] as a thermal-sensitive MRI contrast agent nanomaterial. The application of magnetic NPs for MRI thermometry is an emerging research field,[57−62] and is based on the idea of exploring the influence of the contrast agents on temperature-dependent MRI parameters. If successful, it might be used for identifying ROIs of interest in the body or for monitoring thermal therapy procedures. The topic is beyond the scope of this article, but will be the focus of future research of the group.

4. CONCLUSIONS

Clusters of different sizes were obtained through an ionic force magnetophoresis-mediated phase separation process. In the experiment, a magnetic colloid was placed near a magnet while NaCl was added to disturb the balance of repulsive and attractive interactions between NPs, inducing a "gas-liquid"-like transition that separates different nanostructures. Although this method is not new and has previously been used to obtain monodisperse isolated NPs, here we present evidence that it can effectively tune cluster dimensions. The magnetic field gradient facilitates this process by accelerating separation and allowing clusters containing NPs of distinct diameters to be selected. Multiple techniques were used to confirm these results. Dynamic light scattering showed a decrease in hydrodynamic size with longer separation times. XRD data (using Scherrer's equation and Halder-Wagner formalism) indicated a decrease in crystallite size and confirmed the structure of the cubic spinel ferrite crystal, corroborated by SAED, FFT and IFFT analyses. Transmission electron microscopy revealed that the Mn-ferrite NPs consisted of multicore nanostructures, where the clusters contained NPs of different sizes depending on the separation time. In particular, TEM images demonstrated that, with longer separation times, both the cluster size and the constituent NPs became smaller. This observation aligns with the magnetization data, which showed a considerably decrease in saturation magnetization due to the smaller particles. A core−shell model was used to explain these saturation magnetization values, further supporting the size selection effect. UV−vis spectroscopy, combined with Tauc's analysis, allowed us to determine the band gap energy, which increased as particle size decreased, in agreement with the other techniques analyzes. The size dependence corroborated with confinement effects. The absorbance in the near-infrared region decreased with smaller cluster sizes, which is in agreement with the lower photothermal efficiency measured by both cuvette and droplet methods. MRI characterization revealed a decrease in longitudinal (r_1) and transverse (r_2) relaxivities as the size of the cluster decreased, also indicating a reduction in the sizes of the NPs forming the cluster. The r_2/r_1 ratio indicated these magnetic clusters function as excellent $T2$ contrast agents, as expected for this type of nanomaterial. Importantly, we present a detailed discussion about the origin of the ultrahigh transverse relaxivity and its correlation with both cluster dimension and NP size, using outer sphere theory adapted for clusters. Our analysis showed that the clusters are in the motional average regime. This conclusion was established by evaluating the linear dependence of r_2 on the square of the particle magnetization and the square of the size of the cluster, as predicted by MAR. A comparison between experiment and theory indicated the particle volume fraction of NPs within the cluster. Temperature-dependent relaxivity measurements also confirmed the MAR regime. The results suggest that the multicore magnetic nanocluster holds potential for MRI thermometry. We envision applications in disease diagnosis and real-time monitoring of thermal therapy. In summary, we demonstrate that the size of the multicore Mn-ferrite magnetic cluster is crucial for selecting the best photothermal agent and ultrahigh-relaxivity MRI contrast agent, aiming for new applications as a thermally sensitive MRI contrast agent.

■ ASSOCIATED CONTENT

Supporting Information

The Supporting Information is available free of charge at https://pubs.acs.org/doi/10.1021/acsanm.5c00309.

> Zeta potential data for all samples; XRD pattern for aliquots at 1-h, 2-h, 3-h, 24-h and 48-h separation intervals; crystallite size determination for Mn-ferrite using the Halder−Wagner formalism; detailed examples of TEM images diameter measurement; SEM images and EDS compositional analysis of NP film for 0 h sample; MRI inversion recovery data for *T*1 determination and MRI spin echo data for *T*2 determination of all samples; MRI signal intensities obtained from Spin Echo at different temperatures; *T*1 and *T*2 values obtained from theoretical analysis for all samples and concentrations (PDF)

■ AUTHOR INFORMATION

Corresponding Author

Andris Figueiroa Bakuzis − *Institute of Physics, Federal University of Goiás, Goiânia, Goiás 74690-900, Brazil; CNanoMed, Center for Integrative Nanomedicine Research, Federal University of Goiás, Goiânia, Goiás 74690-631, Brazil;* orcid.org/0000-0003-3366-106X;
Email: bakuzis@ufg.br

Authors

Carlos Eduardo Ribeiro − *Institute of Physics, Federal University of Goiás, Goiânia, Goiás 74690-900, Brazil*
Marcus Vinícius-Araújo − *Institute of Physics, Federal University of Goiás, Goiânia, Goiás 74690-900, Brazil*

Complete contact information is available at:
https://pubs.acs.org/10.1021/acsanm.5c00309

Funding

The Article Processing Charge for the publication of this research was funded by the Coordenacao de Aperfeicoamento de Pessoal de Nivel Superior (CAPES), Brazil (ROR identifier: 00x0ma614).

Notes

The authors declare no competing financial interest.

■ ACKNOWLEDGMENTS

M.V.-A. acknowledges the financial support provided by the Conselho Nacional de Desenvolvimento Científico e Tecnológico - CNPq, grant 380286/2024-6. A.F.B. acknowledges the financial support of the CNPq grants 312458/2021-5 and 405139/2023-3. The authors also thank the LabMic-UFG for access to the Electron Microscopy facilities at UFG, CRTI-UFG for XRD data, FARMATEC for UV−vis, DLS, and zeta potential data, and CNANOMED for MRI data.

■ REFERENCES

(1) Nie, Z.; Petukhova, A.; Kumacheva, E. Properties and emerging applications of self-assembled structures made from inorganic nanoparticles. *Nat. Nanotechnol.* **2010**, *5*, 15−25.

(2) Zhang, C.; Nan, B.; Xu, J.; Yang, T.; Xu, L.; Lu, C.; Zhang, X.-B.; Rao, J.; Song, G. Magnetic-susceptibility-dependent ratiometric probes for enhancing quantitative MRI. *Nat. Biomed. Eng.* **2024**, 1−15.

(3) Zufelato, N.; Aquino, V. R.; Shrivastava, N.; Mendanha, S.; Miotto, R.; Bakuzis, A. F. Heat generation in magnetic hyperthermia by manganese ferrite-based nanoparticles arises from Néel collective magnetic relaxation. *ACS Appl. Nano Mater.* **2022**, *5*, 7521−7539.

(4) Anselmo, A. C.; Mitragotri, S. Nanoparticles in the clinic: An update post COVID-19 vaccines. *Bioeng. Transl. Med.* **2021**, *6*, No. e10246.

(5) Zanganeh, S.; Hutter, G.; Spitler, R.; Lenkov, O.; Mahmoudi, M.; Shaw, A.; Pajarinen, J. S.; Nejadnik, H.; Goodman, S.; Moseley, M. Iron oxide nanoparticles inhibit tumour growth by inducing pro-inflammatory macrophage polarization in tumour tissues. *Nat. Nanotechnol.* **2016**, *11*, 986−994.

(6) Li, J.; Ren, H.; Zhang, Y. Metal-based nano-vaccines for cancer immunotherapy. *Coord. Chem. Rev.* **2022**, *455*, 214345.

(7) Yang, Z.; Gao, D.; Zhao, J.; Yang, G.; Guo, M.; Wang, Y.; Ren, X.; Kim, J. S.; Jin, L.; Tian, Z. Thermal immuno-nanomedicine in cancer. *Nat. Rev. Clin. Oncol.* **2023**, *20*, 116−134.

(8) Rodrigues, H. F.; Capistrano, G.; Bakuzis, A. F. In vivo magnetic nanoparticle hyperthermia: a review on preclinical studies, low-field nano-heaters, noninvasive thermometry and computer simulations for treatment planning. *Int. J. Hyperthermia* **2020**, *37*, 76−99.

(9) Vinícius-Araújo, M.; Shrivastava, N.; Sousa-Junior, A. A.; Mendanha, S. A.; de Santana, R. C.; Bakuzis, A. F. Zn$_X$Mn$_{1-X}$Fe$_2$O$_4$@SiO$_2$: zNd^{3+} Core-Shell Nanoparticles for Low-Field Magnetic Hyperthermia and Enhanced Photothermal Therapy with the Potential for Nanothermometry. *ACS Appl. Nano Mater.* **2021**, *4*, 2190−2210.

(10) Vinícius-Araújo, M.; Sousa, L. R. D.; Santana, R. C. D.; Mendanha, S. A.; Bakuzis, A. F. Erythrocyte membrane-camouflaged magnetic and up/downconverting nanoparticles for photothermal therapy and luminescent nanothermometry. *Appl. Phys. Lett.* **2024**, *125*, 053701.

(11) Sousa-Junior, A. A.; Mello-Andrade, F.; Rocha, J. V. R.; Hayasaki, T. G.; de Curcio, J. S.; Do Carmo Silva, L.; de Santana, R. C.; Lima, E. M.; Cardoso, C. G.; de Paula Silveira-Lacerda, E.; et al. Immunogenic Cell Death Photothermally Mediated by Erythrocyte Membrane-Coated Magnetofluorescent Nanocarriers Improves Survival in Sarcoma Model. *Pharmaceutics* **2023**, *15*, 943.

(12) Toraya-Brown, S.; Sheen, M. R.; Zhang, P.; Chen, L.; Baird, J. R.; Demidenko, E.; Turk, M. J.; Hoopes, P. J.; Conejo-Garcia, J. R.; Fiering, S. Local hyperthermia treatment of tumors induces CD8+ T cell-mediated resistance against distal and secondary tumors. *Nanomedicine* **2014**, *10*, 1273−1285.

(13) Kobayashi, T.; Kakimi, K.; Nakayama, E.; Jimbow, K. Antitumor immunity by magnetic nanoparticle-mediated hyperthermia. *Nanomedicine* **2014**, *9*, 1715−1726.

(14) Hugounenq, P.; Levy, M.; Alloyeau, D.; Lartigue, L.; Dubois, E.; Cabuil, V.; Ricolleau, C.; Roux, S.; Wilhelm, C.; Gazeau, F. Iron oxide monocrystalline nanoflowers for highly efficient magnetic hyperthermia. *J. Phys. Chem. C* **2012**, *116*, 15702−15712.

(15) Soetaert, F.; Kandala, S. K.; Bakuzis, A.; Ivkov, R. Experimental estimation and analysis of variance of the measured loss power of magnetic nanoparticles. *Sci. Rep.* **2017**, *7*, 6661.

(16) Jefremovas, E. M.; Gandarias, L.; Rodrigo, I.; Marcano, L.; Grüttner, C.; García, J. Á.; Garayo, E.; Orue, I.; García-Prieto, A.; Muela, A. Nanoflowers versus magnetosomes: comparison between two promising candidates for magnetic hyperthermia therapy. *IEEE Access* **2021**, *9*, 99552−99561.

(17) Zhou, Z.; Yang, L.; Gao, J.; Chen, X. Structure−Relaxivity Relationships of Magnetic Nanoparticles for Magnetic Resonance Imaging. *Adv. Mater.* **2019**, *31*, 1804567.

(18) Odéen, H.; Parker, D. L. Magnetic resonance thermometry and its biological applications-Physical principles and practical considerations. *Prog. Nucl. Magn. Reson. Spectrosc.* **2019**, *110*, 34−61.

(19) Pan, D.; Caruthers, S. D.; Senpan, A.; Schmieder, A. H.; Wickline, S. A.; Lanza, G. M. Revisiting an old friend: manganese-based MRI contrast agents. *Wiley Interdiscip. Rev.: Nanomed. Nanobiotechnol.* **2011**, *3*, 162−173.

(20) Zhao, Z.; Sun, C.; Bao, J.; Yang, L.; Wei, R.; Cheng, J.; Lin, H.; Gao, J. Surface manganese substitution in magnetite nanocrystals

enhances T 1 contrast ability by increasing electron spin relaxation. *J. Mater. Chem. B* **2018**, *6*, 401−413.

(21) Peters, J. A. Relaxivity of manganese ferrite nanoparticles. *Prog. Nucl. Magn. Reson. Spectrosc.* **2020**, *120*, 72−94.

(22) Rocha, J. V. R.; Krause, R. F.; Ribeiro, C. E.; Oliveira, N. C. D. A.; Ribeiro de Sousa, L.; Leandro Santos Jr, J.; Castro, S. D. M.; Valadares, M. C.; Cunha Xavier Pinto, M.; Pavam, M. V. Near Infrared Biomimetic Hybrid Magnetic Nanocarrier for MRI-Guided Thermal Therapy. *ACS Appl. Mater. Interfaces* **2025**, *17*, 13094−13110.

(23) Leal, M. P.; Rivera-Fernández, S.; Franco, J. M.; Pozo, D.; de La Fuente, J. M.; García-Martín, M. L. Long-circulating PEGylated manganese ferrite nanoparticles for MRI-based molecular imaging. *Nanoscale* **2015**, *7*, 2050−2059.

(24) Pereira, C.; Pereira, A. M.; Fernandes, C.; Rocha, M.; Mendes, R.; Fernández-García, M. P.; Guedes, A.; Tavares, P. B.; Grenèche, J.-M.; Araújo, J. P.; Freire, C. Superparamagnetic MFe2O4 (M = Fe, Co, Mn) Nanoparticles: Tuning the Particle Size and Magnetic Properties through a Novel One-Step Coprecipitation Route. *Chem. Mater.* **2012**, *24*, 1496−1504.

(25) Horta, A. C.; Poças, A.; Amaral, J. S.; Amorim, C. O. Fine-Tuning of Mn-Ferrite nanoparticle size using a Dual-Base coprecipitation method. *Mater. Sci. Eng.* **2025**, *314*, 118058.

(26) Jang, J.-T.; Nah, H.; Lee, J.-H.; Moon, S. H.; Kim, M. G.; Cheon, J. Critical enhancements of MRI contrast and hyperthermic effects by dopant-controlled magnetic nanoparticles. *Angew. Chem., Int. Ed.* **2009**, *48*, 1234−1238.

(27) Zhao, Z.; Zhou, Z.; Bao, J.; Wang, Z.; Hu, J.; Chi, X.; Ni, K.; Wang, R.; Chen, X.; Chen, Z. Octapod iron oxide nanoparticles as high-performance T 2 contrast agents for magnetic resonance imaging. *Nat. Commun.* **2013**, *4*, 2266.

(28) Gossuin, Y.; Martin, E.; Vuong, Q. L.; Delroisse, J.; Laurent, S.; Stanicki, D.; Rousseau, C. Characterization of commercial iron oxide clusters with high transverse relaxivity. *J. Magn. Reson. Open* **2022**, *10*, 100054.

(29) Vuong, Q. L.; Berret, J.-F.; Fresnais, J.; Gossuin, Y.; Sandre, O. A universal scaling law to predict the efficiency of magnetic nanoparticles as MRI T2-contrast agents. *Adv. Healthcare Mater.* **2012**, *1*, 502−512.

(30) Zhou, Z.; Tian, R.; Wang, Z.; Yang, Z.; Liu, Y.; Liu, G.; Wang, R.; Gao, J.; Song, J.; Nie, L.; et al. Artificial local magnetic field inhomogeneity enhances T 2 relaxivity. *Nat. Commun.* **2017**, *8*, 15468.

(31) Mikhaylov, G.; Mikac, U.; Magaeva, A. A.; Itin, V. I.; Naiden, E. P.; Psakhye, I.; Babes, L.; Reinheckel, T.; Peters, C.; Zeiser, R. Ferri-liposomes as an MRI-visible drug-delivery system for targeting tumours and their microenvironment. *Nat. Nanotechnol.* **2011**, *6*, 594−602.

(32) Pöselt, E.; Kloust, H.; Tromsdorf, U.; Janschel, M.; Hahn, C.; Maßlo, C.; Weller, H. Relaxivity optimization of a PEGylated iron-oxide-based negative magnetic resonance contrast agent for T 2-weighted spin−echo imaging. *ACS Nano* **2012**, *6*, 1619−1624.

(33) Massart, R.; Dubois, E.; Cabuil, V.; Hasmonay, E. Preparation and properties of monodisperse magnetic fluids. *J. Magn. Magn. Mater.* **1995**, *149*, 1−5.

(34) Carriao, M.; Neto, K. S.; Bakuzis, A. Mass magnetophoretic experiment applied to the separation of biocompatible magnetic nanoparticles with potential for magnetohyperthermia. *J. Phys. D: Appl. Phys.* **2014**, *47*, 025003.

(35) Bakuzis, A. F.; Branquinho, L. C.; E Castro, L. L.; E Eloi, M. T. D. A.; Miotto, R. Chain formation and aging process in biocompatible polydisperse ferrofluids: Experimental investigation and Monte Carlo simulations. *Adv. Colloid Interface Sci.* **2013**, *191*, 1−21.

(36) Aquino, V.; Figueiredo, L.; Coaquira, J.; Sousa, M.; Bakuzis, A. Magnetic interaction and anisotropy axes arrangement in nanoparticle aggregates can enhance or reduce the effective magnetic anisotropy. *J. Magn. Magn. Mater.* **2020**, *498*, 166170.

(37) Aono, C.; Aquino, V.; Bakuzis, A.; Miotto, R. Kinetic Monte Carlo Approach as a Tool for the Study of Magnetic Hyperthermia Efficiency. *J. Phys. Chem. C* **2025**, *129*, 927−939.

(38) Tauc, J. Optical properties and electronic structure of amorphous Ge and Si. *Mater. Res. Bull.* **1968**, *3*, 37−46.

(39) Roper, D. K.; Ahn, W.; Hoepfner, M. Microscale heat transfer transduced by surface plasmon resonant gold nanoparticles. *J. Phys. Chem. C* **2007**, *111*, 3636−3641.

(40) Pasciak, A.; Marin, R.; Abiven, L.; Pilch-Wróbel, A.; Misiak, M.; Xu, W.; Prorok, K.; Bezkrovnyi, O.; Marciniak, Ł.; Chanéac, C. Quantitative comparison of the light-to-heat conversion efficiency in nanomaterials suitable for photothermal therapy. *ACS Appl. Mater. Interfaces* **2022**, *14*, 33555−33566.

(41) Haase, A. Snapshot FLASH MRI. Applications to T1, T2, and chemical-shift imaging. *Magn. Reson. Med.* **1990**, *13*, 77−89.

(42) Jivan, A.; Horsfield, M.; Moody, A.; Cherryman, G. Dynamic T1Measurement Using Snapshot-FLASH MRI. *J. Magn. Reson.* **1997**, *127*, 65−72.

(43) Deichmann, R.; Haase, A. Quantification of T1 values by SNAPSHOT-FLASH NMR imaging. *J. Magn. Reson.* **1992**, *96*, 608−612.

(44) Tang, Z.; Sorensen, C.; Klabunde, K.; Hadjipanayis, G. Size-dependent Curie temperature in nanoscale $MnFe_2O_4$ particles. *Phys. Rev. Lett.* **1991**, *67*, 3602.

(45) Verde, E. L.; Landi, G. T.; Carrião, M.; Drummond, A. L.; Gomes, J.; Vieira, E.; Sousa, M.; Bakuzis, A. F. Field dependent transition to the non-linear regime in magnetic hyperthermia experiments: Comparison between maghemite, copper, zinc, nickel and cobalt ferrite nanoparticles of similar sizes. *AIP Adv.* **2012**, *2*, 032120.

(46) Coey, J. M.. *Magnetism and magnetic materials*; Cambridge University Press, 2010.

(47) Brabers, V. Comment on "Size-dependent Curie temperature in nanoscale $MnFe_2O_4$ particles". *Phys. Rev. Lett.* **1992**, *68*, 3113.

(48) Tan, S. T.; Chen, B. J.; Sun, X. W.; Fan, W. J.; Kwok, H. S.; Zhang, X. H.; Chua, S. J. Blueshift of optical band gap in ZnO thin films grown by metal-organic chemical-vapor deposition. *J. Appl. Phys.* **2005**, *98*, 013505.

(49) Singh, J. P.; Srivastava, R. C.; Agrawal, H. M.; Giri, P. K.; Goswami, D. K.; Perumal, A.; Chattopadhyay, A. Optical Behaviour of Zinc Ferrite Nanoparticles. *AIP Conf. Proc.* **2010**, *1276*, 137−143.

(50) Allan, G.; Delerue, C. Confinement effects in PbSe quantum wells and nanocrystals. *Phys. Rev. B* **2004**, *70*, 245321.

(51) Xia, C.; Wu, W.; Yu, T.; Xie, X.; van Oversteeg, C.; Gerritsen, H. C.; de Mello Donega, C. Size-Dependent Band-Gap and Molar Absorption Coefficients of Colloidal $CuInS_2$ Quantum Dots. *ACS Nano* **2018**, *12*, 8350−8361.

(52) Mosabberul Haque, M.; Rahman, A.; Shafiul Islam Shahin, M.; Ahsan Habib, M.; Abu Rayhan Khan, M.; Mahiuddin, M.; Uddin Monir, M.; Md. Rezaul Karim, K. Manganese doped copper ferrite nanoparticles: A promising approach for organic dye elimination under light irradiation. *Results Chem.* **2024**, *7*, 101509.

(53) Yang, A.; Chinnasamy, C. N.; Greneche, J. M.; Chen, Y.; Yoon, S. D.; Chen, Z.; Hsu, K.; Cai, Z.; Ziemer, K.; Vittoria, C.; Harris, V. G. Enhanced Néel temperature in Mn ferrite nanoparticles linked to growth-rate-induced cation inversion. *Nanotechnology* **2009**, *20*, 185704.

(54) Vamvakidis, K.; Katsikini, M.; Sakellari, D.; Paloura, E. C.; Kalogirou, O.; Dendrinou-Samara, C. Reducing the inversion degree of $MnFe_2O_4$ nanoparticles through synthesis to enhance magnetization: evaluation of their 1H NMR relaxation and heating efficiency. *Dalton Trans.* **2014**, *43*, 12754−12765.

(55) Aquino, V.; Vinícius-Araújo, M.; Shrivastava, N.; Sousa, M.; Coaquira, J.; Bakuzis, A. Role of the fraction of blocked nanoparticles on the hyperthermia efficiency of Mn-based ferrites at clinically relevant conditions. *J. Phys. Chem. C* **2019**, *123*, 27725−27734.

(56) Holz, M.; Heil, S. R.; Sacco, A. Temperature-dependent self-diffusion coefficients of water and six selected molecular liquids for calibration in accurate 1H NMR PFG measurements. *Phys. Chem. Chem. Phys.* **2000**, *2*, 4740−4742.

(57) Chalise, D.; Cahill, D. G. Highly Sensitive and High-Throughput Magnetic Resonance Thermometry of Fluids Using Superparamagnetic Nanoparticles. *Phys. Rev. Appl.* **2023**, *19*, 014055.

(58) Hankiewicz, J.; Stoll, J.; Stroud, J.; Davidson, J.; Livesey, K.; Tvrdy, K.; Roshko, A.; Russek, S.; Stupic, K.; Bilski, P.; Camley, R.; Celinski, Z. Nano-sized ferrite particles for magnetic resonance imaging thermometry. *J. Magn. Magn. Mater.* **2019**, *469*, 550−557.

(59) Hankiewicz, J.; Celinski, Z.; Stupic, K.; Anderson, N.; Camley, R. Ferromagnetic particles as magnetic resonance imaging temperature sensors. *Nat. Commun.* **2016**, *7*, 12415.

(60) Stroud, J.; Hao, Y.; Read, T. S.; Hankiewicz, J. H.; Bilski, P.; Klodowski, K.; Brown, J. M.; Rogers, K.; Stoll, J.; Camley, R. E.; Celinski, Z.; Przybylski, M. Magnetic particle based MRI thermometry at 0.2 and 3 T. *Magn. Reson. Imaging* **2023**, *100*, 43−54.

(61) Lachowicz, D.; Stroud, J.; Hankiewicz, J. H.; Gassen, R.; Kmita, A.; Stepień, J.; Celinski, Z.; Sikora, M.; Zukrowski, J.; Gajewska, M.; Przybylski, M. One-Step Preparation of Highly Stable Copper−Zinc Ferrite Nanoparticles in Water Suitable for MRI Thermometry. *Chem. Mater.* **2022**, *34*, 4001−4018.

(62) Zhang, Y.; Guo, S.; Zhang, P.; Zhong, J.; Liu, W. Iron oxide magnetic nanoparticles based low-field MR thermometry. *Nanotechnology* **2020**, *31*, 345101.